

Influence of Layer Thickness on the Drying of Lithium-Ion Battery Electrodes—Simulation and Experimental Validation

Jana Kumberg,* Michael Baunach, Jochen C. Eser, Andreas Altvater, Philip Scharfer, and Wilhelm Schabel

In this work, a detailed study of the drying of battery electrodes of different thicknesses is presented. A mathematical model to calculate the solvent loading and film temperature over the drying time is experimentally validated. The model is based on a first study presenting a simulation model to predict the drying course when linear drying kinetics prevail and no resistance exists for solvent transport within the film. To shed some light on the drying behavior of electrode films with different thicknesses, the start of capillary pore emptying is observed using a digital microscope. In the experiments, an onset of capillary transport even before the end of film shrinkage is observed for the electrode films with thicknesses above state-of-the-art-thickness. A clusterwise drying behavior becomes more distinct for thicker electrodes, with large areas of dry and wet capillaries next to each other, compared to a more homogenous drying of the thin electrodes. Based on these findings, the linear model is extended to consider transport limitations within the porous electrode film in the form of a moving drying front. The experiments show an increasing deviation from the linear model with increasing electrode thickness and the extended simulation, which considers transport resistances within the film, shows good agreement.


interface has also been observed for drying of electrodes with increasing film thickness/area weight.^[3] The processing of electrodes with higher thicknesses, though, is promising, as it improves the ratio between inactive components such as the current collector to the active components of the battery. To find processing routes that allow the processing of thicker electrodes with a homogenous distribution of additives, the drying step and its influences have to be studied and understood in detail. The literature shows a lot of modeling work focusing on the simulation of the drying of porous systems. At the beginning, the drying of a particulate film with a sufficiently high solvent loading can be described like the drying of a pure solvent film. The particles are distanced far from each other, and sufficient solvent is available at the film surface. The solvent evaporates at a constant drying rate and the film shrinks accordingly up to the point where the particles are closest together and the film

1. Introduction

The drying step of particulate electrode coatings used in lithium-ion batteries highly effects the formation of the microstructure, with a differing amount of additives such as binder and carbon black accumulating at the electrode surface depending on the drying conditions.^[1,2] A binder depletion at the particle–substrate

stops shrinking at the end of film shrinkage (EOF). The mechanism gets more complicated when the particles move closer together because capillary forces start to become relevant. The existence of capillary transport governing the drying behavior of unsaturated porous systems was first identified by Comings and Sherwood.^[4] This work explains that small menisci at the surface of a porous film pump the liquid of larger pores with big menisci to the film surface as long as they are interconnected. This leads to a prolonged constant drying rate even after the end of film shrinkage, which is controlled by the surrounding air conditions. Only at the drying stage, where no small surface menisci are available, will the surface menisci retreat into the film and the drying rate decrease. Based on these findings, models were evolved to describe the heat and mass transport of porous systems during drying. Krischer summarized these models and proposed a “moving drying front model” that considers the resistance of the porous system, which starts to play a role as soon as the smallest menisci retreat into the film, leading to the so-called falling rate period with a decreasing drying rate. A resistance for both heat and mass transport, which is dependent on the distance between the uppermost menisci and the film surface, was introduced.^[5] Schlünder showed that for

J. Kumberg, M. Baunach, J. C. Eser, A. Altvater, Dr. P. Scharfer, Prof. W. Schabel
Institute of Thermal Process Engineering (TVT)
Thin Film Technology (TFT)
Karlsruhe Institute of Technology (KIT)
Straße am Forum 7, Karlsruhe D-76131, Germany
E-mail: jana.kumberg@kit.edu

 The ORCID identification number(s) for the author(s) of this article can be found under <https://doi.org/10.1002/ente.202100013>.

© 2021 The Authors. Energy Technology published by Wiley-VCH GmbH. This is an open access article under the terms of the Creative Commons Attribution License, which permits use, distribution and reproduction in any medium, provided the original work is properly cited.

DOI: 10.1002/ente.202100013

some material systems a constant drying rate could be upheld until a wet surface area of only 1% was reached, as long as the capillaries were finely and evenly distributed and the ratio of the capillary radius to the viscous boundary layer thickness was small.^[6] The moving drying front model was later critically reviewed by Schlünder: He argued that due to small temperature differences within the drying film, with a slightly warmer surface and a cooler center, a vapor diffusion to the bottom would result. The direction of this vapor diffusion would exclude the possibility of retreating capillary menisci and drying by vapor diffusion. He postulated that even during the falling rate period, the solvent was transported to the surface by capillary conduction. Instead of retreating capillaries leading to a decreasing drying rate, he proposed that at one point during drying, the evaporated water stream would split. One part would leave the product and the other part would circulate back to recondensate at the film bottom, comparable to a “heat pipe,” which would result in a more homogenous temperature.^[7] For a deep understanding of the complex system of a capillary network, and to exactly describe the transport phenomena connected to this, new modeling approaches were needed. Prat was the first to implement the invasion percolation model to describe the drying behavior of the capillary network within a porous system.^[8] Modeling has evolved far from that point on, with the current pore network modeling being able to describe even complex pore structures of different pore sizes.^[9–15] Although modeling is well advanced, it still requires a lot of computing power and information on the actual film morphology to predict the drying behavior of realistic pore networks.

As a feasible way to predict the drying behavior of battery electrodes while circumventing huge computing efforts, a simple simulative model was used and experimentally validated based on solvent-loading drying curves.^[16] In the model it is assumed that solvent evaporation would solely take place at the electrode surface where it is transported by capillary pressure. For the low electrode thicknesses examined there, it was shown that no resistance within the film for mass and heat transport has to be considered, as was justified by evaluating the heat and mass transport Biot numbers. Because the Biot numbers linearly increase with the film thickness, the film resistance gains in importance at higher film thicknesses. For this reason, it has to be verified whether the transport resistances within the porous structure of a lithium-ion battery electrode can be neglected for higher electrode thicknesses as well.

2. Experimental Section

To obtain gravimetric drying curves, the experimental setup using the stationary comb nozzle dryer which was introduced in detail in a previous work was used and is explained here in short.^[16] In a second experiment, which was also conducted using the comb nozzle dryer, the pore breakthrough to the film bottom was observed. All slurries used in the experiments were mixed using the same procedure and composition. All experiments were repeated at least three times. Altogether, four different dry electrode thicknesses were investigated.

Table 1. Composition of the dry electrode.

Material	Mass fraction x dry electrode [wt%]
Graphite	93
Carbon black	1.4
CMC	1.87
SBR	3.73

2.1. Slurry Preparation

The slurry was prepared using a dissolver (Dispermat CN10, VMA Gretzmann, Germany), so slurries with a dry mass of 43 wt% resulted. A dry mixing step for graphite (SMGA, Hitachi Chemical Co. Ltd., Japan) and carbon black (Super C65, Timcal, Switzerland) for 10 min at 200 rpm was conducted before the actual wet mixing with a CMC solution (MAC500LC as purchased, Nippon Paper industries, Japan). The main mixing step was performed for 45 min at 1500 rpm while degassing and cooling the slurry. After the main mixing step, styrene butadiene rubber (SBR) was added to the slurry and mixed under moderate settings (10 min at 500 rpm). That resulted in a dry electrode with the composition summarized in **Table 1**.

2.2. Gravimetric Drying Curves

For measuring gravimetric drying curves, a comb nozzle dryer supplemented by a setup to measure weight and temperature changes during drying was used, as shown in **Figure 1**. Between the dryer hood at the top and a heating plate at the bottom, wet electrode films were coated on copper foil as a substrate, fixed in a tensioned frame that stood on top of a precision balance (Sartorius MC1 LC12005). The temperature of the supply and exhaust air nozzles from the dryer was regulated as well as the volume flow of air. The heat and mass transfer coefficients can be adjusted by regulating the flow rate as explained in more detail in a previous work.^[16] Thus, the drying conditions from the top can be controlled. The heat input from the bottom was adjusted by the heating plate, which ensures heat transfer by free convection, because an air gap between the film and plate is set accordingly. The temperatures of the film at the position of the substrate and of the drying air were measured during the experiment using thermocouples of type T. To enable the coating step, the balance with the electrode film can be moved down to stand on top of an intermediate plate. Thus, the coating can be performed by a coating knife, which is attached via a coating arm to a linear drive controlled by a stepper motor. An independent determination of the films' dry area weight was undertaken after the experiment. The films were taken from the experimental setup and weighed. The dry area weight was obtained by subtracting the weight of the copper foil and the equilibrium amount of sorbed water in the film in the surrounding ambient air during the measurement from the measured value. The equilibrium water loading of the film was calculated as proposed by Eser et al. for sorption of water in battery electrodes, which was used for the model used in the previous work as well as in this work.^[16,17] The amount of sorbed water in equilibrium to ambient air was calculated to lie between 0.3 and 1.3 g m⁻² depending

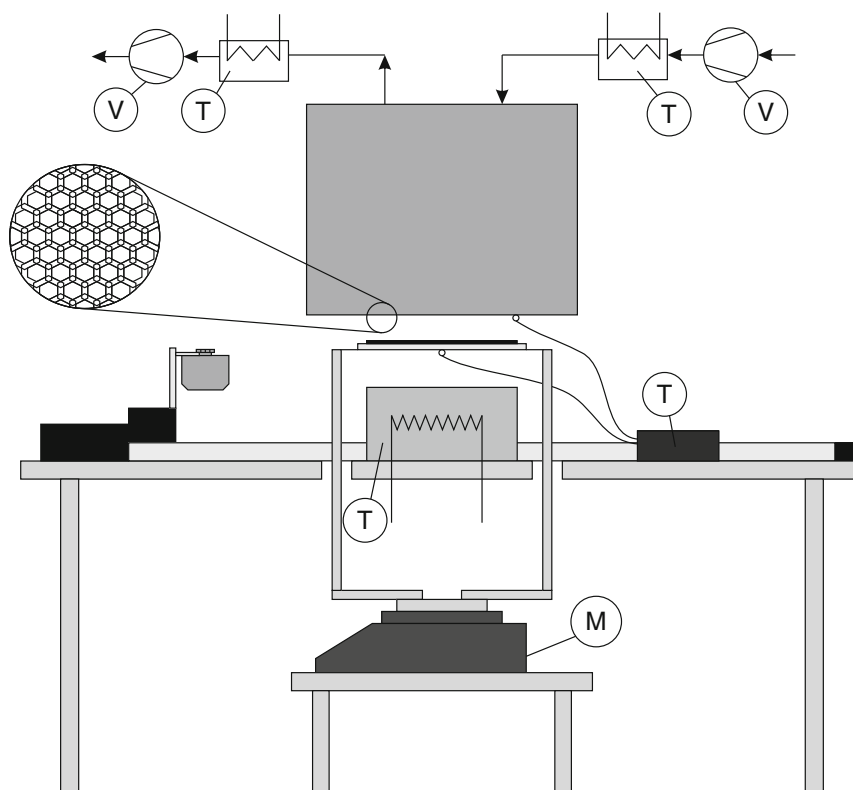


Figure 1. Comb nozzle dryer (CN Drying Technology) and the setup for gravimetric drying curves. The wet film is located in a tensioned frame, which stands on top of a scale. The mass and the temperature are recorded during drying, which is conducted by the drying hood on top.

on the film thickness. The film thickness of each film was measured independently at least at ten positions using a measuring probe (Mitutoyo Meßgeräte Leonberg GmbH, Germany).

2.3. Investigation of the Pore-Emptying Behavior

For investigating the first breakthrough of pores to the film bottom, a digital microscope (Keyence, VHX-6000) was used. The objective lens was fixed beneath the table, which had a round cut-out as shown in **Figure 2**. The electrode film was coated onto a glass substrate using a coating knife with an automated coating arm. A video was taken from the bottom of the electrode while the film temperature was tracked using a thermocouple that was attached to the bottom of the glass substrate. The film thickness was measured afterward at least at ten positions of the film.

An overview of the experimental settings for both the gravimetric measurement and the experiment using the digital microscope is given in **Table 2**. Because the observation of the beginning of pore emptying was undertaken from the bottom of the film, no heating plate in this position was used.

3. Simulation Model

For simulative validation, a model proposed in a previous work was used.^[16] To account for transport resistances within the film

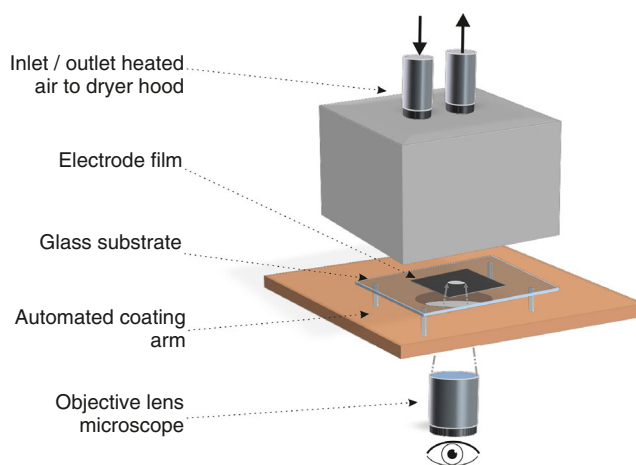


Figure 2. Experimental setup for the observation of the pore emptying using a digital microscope.

during drying of thicker electrodes, the approach proposed by Krischer and further developed by Schlünder was introduced into the simulation.^[5,6] At one point during drying, the meniscus of the uppermost capillary recedes into the film and mass and heat transfer are not solely governed by the drying conditions outside the film, as shown schematically in **Figure 3**. The film moves inward like a moving drying front with the distance to the film surface given as $s(t)$.

Table 2. Overview of the experimental settings for the gravimetric and the digital microscope experiment.

	Dryer temperature T_{dryer} [°C]	Temperature heating plate $T_{\text{heating plate}}$ [°C]	Experimental heat transfer coefficient α_{exp} [W m ⁻² K ⁻¹]	Coating area A_{el} [mm ⁻²]	Substrate [-]
Gravimetric measurement	80	50	determined for each m	90 × 90	Copper foil
digital microscope experiment	86	–	36	90 × 90	Glass plate

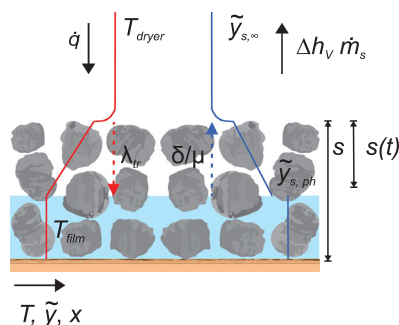


Figure 3. Moving drying front model as proposed by Krischer.^[5]

Within the porous structure of the film, the heat and mass transfer decreases. Therefore, a term for the transport within the film is introduced in the equation of heat input from the top and the evaporating mass flow, as given in Equation (1) and (2).

$$\dot{q}_{\text{top}} = K_A \frac{1}{\frac{1}{\alpha_{\text{top}}} + \frac{s(t)}{\lambda_{\text{tr}}}} (T_{\text{dryer}} - T_{\text{film}}) \quad (1)$$

$$\dot{m}_s = K_S \tilde{M}_s \frac{1}{\frac{1}{\beta_{s,\text{air}}} + \frac{s(t)}{\delta_{\text{tr}}}} \tilde{\rho}_{\text{air}}(T_{m,t}) (\tilde{y}_{s,\text{ph}} - \tilde{y}_{s,\infty}) \quad (2)$$

The heat transfer coefficient within the film as well as the diffusion coefficient can be calculated according to Zehner–Bauer–Schlünder knowing the porosity of the film.^[18] As the diffusion of water vapor within graphite can be assumed to be negligible, the diffusion coefficient within the drying front is dependent on the film's porosity ϵ and the diffusion coefficient of water in air $\delta_{\text{water,air}}$ as given in Equation (3).

$$\delta_{\text{tr}} = \delta_{\text{water,air}} (1 - \sqrt{1 - \epsilon}) \quad (3)$$

For the simulation, it is assumed that the menisci retreat into the film after the theoretical EOF shrinkage is reached in the drying curve.

The solvent loading at the EOF shrinkage can be calculated assuming that at this moment the particles have reached their final porosity and all pore space is filled with the solvent. Then, the theoretical solvent loading at the EOF shrinkage X_{EOF} is dependent on experimentally determined properties, namely, the film thickness h_{film} , the dry mass of the electrode

M_{el} , and the electrode area A_{el} as well as the solid density of the dry electrode, with $\rho_{\text{el}} = 2136 \text{ kg m}^{-3}$ as shown in Equation (4).

$$X_{\text{EOF}} = \frac{\rho_s \epsilon h_{\text{film}} A_{\text{el}}}{M_{\text{el}}} \quad (4)$$

The time until the EOF shrinkage t_{EOF} is reached can be determined according to Equation (5) with knowledge of the drying rate, the initial solvent loading $X(t=0)$, the dry area weight of the electrode m , and the solvent loading at the EOF shrinkage.

$$t_{\text{EOF}} = \frac{(X(t=0) - X(t_{\text{EOF}}))m}{\dot{m}_s} \quad (5)$$

The distance of the moving drying front $s(t)$ is calculated for each time step, being the difference between the dry film thickness and the water film height at the corresponding solvent loading $X(t)$, which can also be calculated according to Equation (10), assuming the moving drying front.

4. Results and Discussion

A gravimetric setup as explained in more detail in the Experimental Section was used to investigate the drying behavior of battery electrodes of different thicknesses.^[16] These experiments are compared to the drying course recorded by a digital microscope (see the subsection Investigation of the Pore Emptying Behavior) and the calculated drying curve.

4.1. Experimental Drying Curves of Electrodes with Differing Area Weights

Gravimetric drying curves, consisting of the solvent loading as well as the film temperature over time were recorded for four different electrode thicknesses at comparable drying conditions. A summary of the dry film properties thickness, area weight, and porosity sorted by the dry area weight m of the respective electrodes is given in Table 3. All values are averaged values of the film properties of the experiments, which were repeated at least three times. The films themselves deviate in their film thickness, with a growing standard deviation with increasing area weight, which lies between 6 and 8% of the average film thickness. The solvent

Table 3. Overview of the film properties of the gravimetric experiments for the four electrodes, sorted by their dry area weight m .

Dry area weight m [g m ⁻²]	Theoretical capacity c_A [mA h cm ⁻²]	Dry electrode film thickness h_{film} [μm] ^{a)}	Standard deviation single electrode [μm] ^{b)}	Porosity ϵ	Solvent loading @ EOF $X_{S,\text{EOF}}$ [g g ⁻¹]
$m_1 = 72 \pm 5$	2.4 ± 0.2	83 ± 5	± 5	0.584	0.658
$m_2 = 160 \pm 12$	5.4 ± 0.4	176 ± 13	± 13	0.575	0.632
$m_3 = 201 \pm 1$	6.8 ± 0.0	220 ± 1	± 18	0.570	0.621
$m_4 = 278 \pm 10$	9.4 ± 0.3	299 ± 16	± 24	0.562	0.600

^{a)}The indicated errors refer to the repetition of the experiment; ^{b)}The indicated errors refer to the standard deviation of a single film.

loading at the theoretical end of film shrinkage is calculated from the film properties according to Section 3, Simulation Model. The porosity decreases with growing area weight, which might be an effect of particles having more time to ideally align themselves. As a result, the solvent loading at the theoretical end of film shrinkage decreases with a growing film thickness. The experimentally determined area weight as well as the solvent loading and temperature over time is shown in **Figure 4**. The course of the area weight over time (Figure 4, top) shows an almost identical slope for all four area weights in the beginning due to the similar drying rate at the beginning of drying. All four courses stop at their respective dry area weight. The graph of the solvent loading over drying time (Figure 4, bottom) shows that all four electrodes start at a similar solvent loading. As expected, the solvent loading of the electrode with the lowest area weight reaches the point of no residual solvent loading first; the films of higher area weights require more time to dry. The course of solvent loading over time seems to be linear for the electrode with the lowest area weight, although one might assume a deviation from the linear course for the thicker electrodes. This will be discussed in more detail along with the simulation in Section 2.3, Experimental Validation of the Simulation Model. Nevertheless, all four electrodes show a consistently high drying rate, even after the theoretical end of film shrinkage, represented by the characteristic solvent loading X_{EOF} . Regarding the temperature course, the steady state temperature at the beginning of drying is almost identical for all area weights. The area weight of the electrodes does not seem to affect the time needed to reach the steady state temperature because all four temperature curves reach the steady state temperature after an initial heating phase of ≈ 20 s. The differences of the temperature curves begin when the respective solvent loading course has reached values close to zero. At this point, the heating phase of the respective electrode starts and the film heats up, until it reaches the equilibrium temperature. The slopes of the temperature curves are quite different, whereas

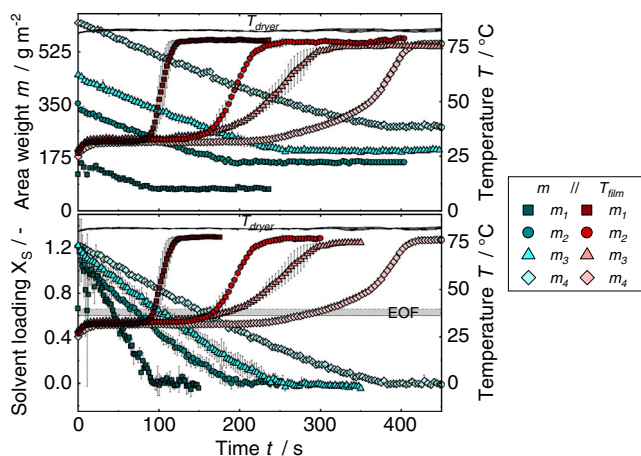


Figure 4. Experimental drying curves of electrodes with four different film thicknesses. Film properties are summarized according to the dry film area weight m in Table 3. The course of area weight (top) and solvent loading (bottom) as well as the film temperature over time are shown for the respective electrodes. For better visualization, the experimental data were shortened in the bottom graph and the amount of experimental data was reduced to every fourth data point in both diagrams.

the end temperatures of all films are similarly close to the adjusted dryer temperature.

The gravimetric drying curves indicate that capillary mass transport of water to the film surface is responsible for a high drying rate long after the end of film shrinkage, although the data show the nonlinear behavior for the drying rates at higher electrode thickness. Our study conducted an experimental investigation of the pore-emptying behavior to evaluate at what point during drying and to what extent capillary transport influences the drying behavior of electrodes of different thicknesses.

4.2. Investigation of Pore-Emptying Behavior

A digital microscope was used in the drying setup to visualize the pore emptying at the bottom of the electrode film. For this purpose, the electrode film was coated onto a transparent glass substrate. The film temperature was measured simultaneously by a thermocouple that was placed at the bottom of the substrate. Electrode films of different area weights are compared in regard to the breakthrough of the first pore and the homogeneity of the pore emptying.

4.2.1. Observation of First Empty Pore Breaking Through

The electrode bottom was filmed during drying and the point of time when the first pore broke through to the substrate was determined. In **Figure 5**, pictures of an electrode with an area weight of $\approx 67 \text{ g m}^{-2}$ during drying are shown. At the beginning, a homogenous wet film is visible (Figure 5a). After 45 s of drying time, the first pore breaks through to the bottom of the electrode film (Figure 5b), and 5 s later, homogeneously distributed empty pores are visible all over the film, which steadily increase in number (Figure 5c–e). The number of pores increases further until there is no visible change present in the electrode film.

4.2.2. Experimental and Simulated Drying Curves of the Electrodes for the Digital Microscope

To determine whether the film thickness influences the point of breakthrough of air to the electrode bottom and the emptying behavior itself, the experiment was conducted for all four different electrode thicknesses. The dryer was set to the same settings as for the gravimetric setup (see Table 2 in the Experimental Section), but without the heating plate, due to the new experimental setup. The use of a transparent glass substrate instead of copper foil results in a different heat capacity of the substrate. The drying rate was determined based on simultaneous measurement of the film temperature. As shown in a previous work, the course of the film temperature and the solvent loading can be predicted for the smallest electrode thickness, knowing the heat transfer coefficient.^[16] Therefore, the heat transfer coefficient was determined by adjusting the simulated film temperature until it matched the experimental course. The resulting simulated temperature as well as the experimental course is shown in **Figure 6**. The time scale with the corresponding pore-emptying stage is shown in Figure 5, as well as the experimentally determined first empty pore and the theoretical end of film shrinkage derived from the simulation.

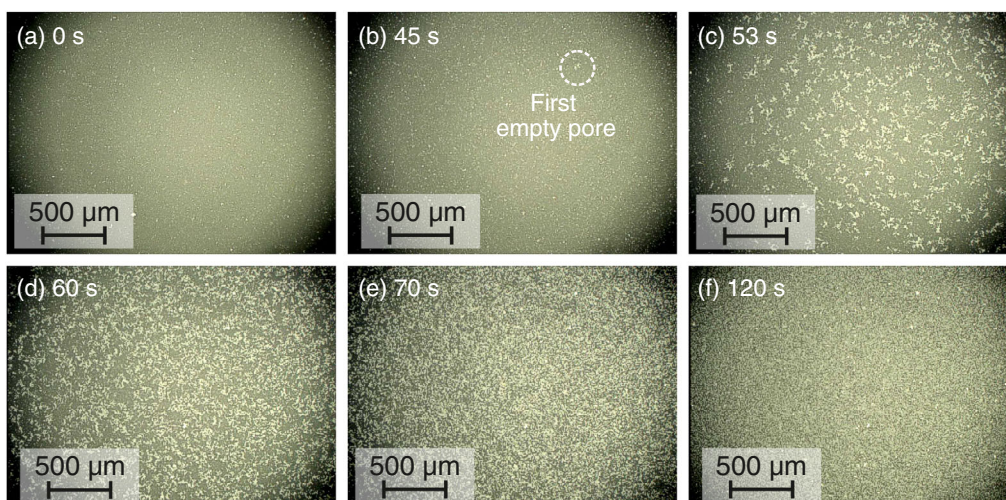


Figure 5. Progression of pore emptying of an electrode film with an area weight of 67 g m^{-2} viewed from below. The drying time at which the pictures are taken increases from a) 0 s to f) 120 s. b) The first empty pore observed after 45 s of drying time is highlighted.

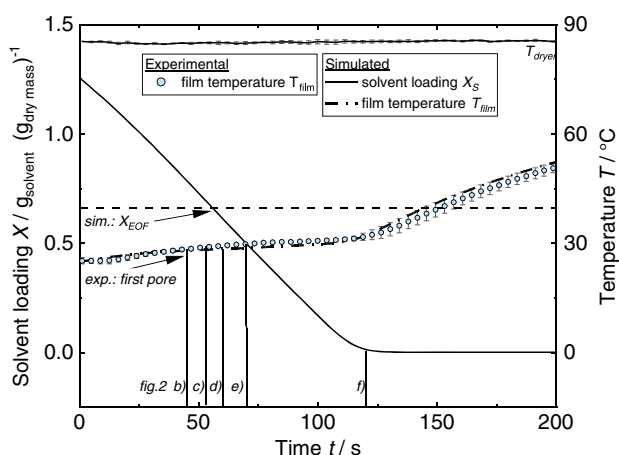


Figure 6. Experimental temperature curve recorded by the thermocouple during the experiment using the digital microscope. To extract a value for the heat transfer coefficient and the theoretical end of film shrinkage during the experiments, a fit between simulated and experimental data was conducted. Therefore, the simulation was adapted to the new experimental setup with the glass plate as substrate and the missing heating plate at the bottom.

All experiments were conducted with the same setup and a measured convective heat transfer coefficient at the top of $36 \text{ W m}^{-2} \text{ K}^{-1}$, which was used for the determination of the end of film shrinkage of all film thicknesses (see Section 3). The end of film shrinkage is therefore a theoretical value that is derived from the experimental measurements of the drying curves in terms of the film temperature. With knowledge of the drying rate, the end of film shrinkage can be determined as described in Section 3 (Simulation Model, Equation (4) and (5)). A direct measurement of the change of film height is not possible without interfering with the drying process itself in this experimental setup. In the literature, measurements of the change of film height of NMP-based anode slurries up to

the end of film shrinkage have been described using a 2D laser.^[19] A coincidence of the theoretical and the experimental end of film shrinkage has been found for the thin electrode films investigated there. Moreover, the onset of pore depletion was investigated and it was found that pore emptying would start at the end of film shrinkage when polyhedral graphite was used and drying rates up to $1.2 \text{ g m}^{-2} \text{ s}^{-1}$ were set. This is in good agreement with the data presented here, where the maximum drying rate was set to $1.14 \text{ g m}^{-2} \text{ s}^{-1}$.

4.2.3. Comparison of Experimental Pore Breakthrough and Calculated EOF Shrinkage

The experimentally determined time until the first pore breaks through to the bottom of the film $t_{\text{first pore, exp}}$ was compared to the time until the theoretical end of film shrinkage $t_{\text{EOF, theo}}$ was reached. These times are shown for the four different electrode area weights in **Figure 7**.

For the lowest area weight, the time of the theoretical EOF and that of the first empty pore almost coincide. With increasing area weight, there is a growing deviation between the appearance of the first empty pore and the EOF shrinkage with the empty pore breaking through, long before the end of film shrinkage is reached. The time difference grows with the film thickness, which means that the beginning of pore emptying starts earlier the thicker the electrode layer is. A reason for an earlier start of the capillary conduction might be a consolidation layer, with large particles moving together at the top of the film during drying, resulting in smaller pores r_c at the top of the film and leading to a higher capillary pressure $p_c = \frac{2\gamma \cos \theta}{r_c}$, γ thereby being the interfacial tension and θ being the wetting angle. The same capillary pressure seems to build up only at the end of film shrinkage for thin electrodes, when the particles move together as close as possible.

To evaluate whether a consolidation of particles at the film surface is possible, the consolidation factor K_C was calculated, as

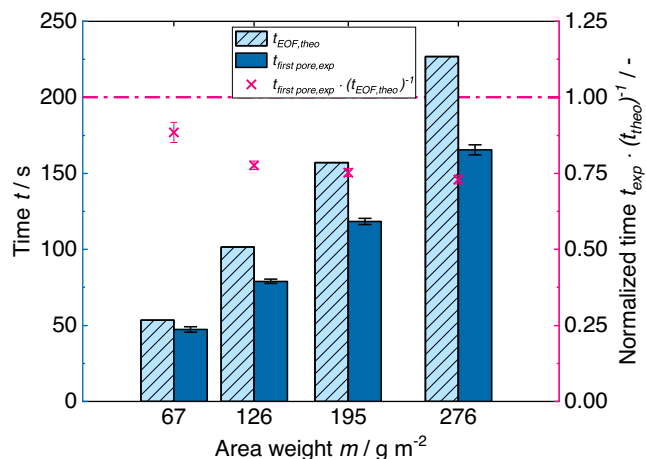


Figure 7. Comparison of the theoretical EOF shrinkage with the experimentally determined first pore which breaks through to the film bottom in dependency of the respective area weight.

shown by Baunach et al.^[20] For systems with lower volume ratios of particles, a drying regime map can be set up to discern where particles are likely to be positioned during drying. The drying regime map is divided into a sedimentation, an evaporation, and a diffusion regime.^[21,22] Therefore, the sedimentation speed u_{sed} and diffusion velocity u_{diff} as driving forces for the particles to move to the substrate in relation to the evaporation rate u_{evap} as driving force for the particles to accumulate at the film surface were considered, resulting in the consolidation factor K_C according to Equation (6).

$$K_C = \frac{u_{\text{diff}} + u_{\text{sed}}}{u_{\text{evap}}} \quad (6)$$

The sedimentation speed was calculated according to Stokes (Equation (7)). Therein, r_p is the mean particle radius, with a value of $9.2 \mu\text{m}$, g the gravitational acceleration, ρ_p is the particle density 2260 kg m^{-3} , and ρ_s is the density of the carboxymethyl cellulose (CMC) solution 1002 kg m^{-3} . η is the dynamic viscosity of the CMC solution with its zero-shear viscosity determined with the cross-model, being 21.7 Pa s .

$$u_{\text{sed}} = \frac{2r_p^2 g (\rho_p - \rho_s)}{9\eta} \quad (7)$$

The diffusion velocity is determined with the diffusion coefficient of a graphite particle within the CMC solution $\delta_{p,\text{CMC-solution}}$ according to Stokes–Einstein (see Equation (8)).

$$\delta_{p,\text{CMC-solution}} = \frac{k_B T}{6\pi\eta r_p} \quad (8)$$

T is the temperature, in kelvin, and k_B is the Boltzmann constant. The diffusion velocity was estimated according to Baunach et al. following Equation (9).^[20]

Table 4. Comparison of the driving forces on a graphite particle during the described drying process with the maximum distance one single particle might cover based on the conditions in the gravimetric experiment.

Dry area weight m [g m^{-2}]	Diffusion velocity u_{diff} [$\mu\text{m s}^{-1}$]	Sedimentation speed u_{sed} [$\mu\text{m s}^{-1}$]	Evaporation rate u_{evap} [$\mu\text{m s}^{-1}$]	Consolidation factor K_C [-]	$\frac{h_0 - h_{\text{EOF}}}{d_p}$ [-]
$m_1 = 72 \pm 5$	7.5×10^{-9}	0.011	0.894	0.0120	2.2
$m_2 = 160 \pm 12$	8.0×10^{-9}	0.011	1.055	0.0101	5.1
$m_3 = 201 \pm 1$	8.1×10^{-9}	0.011	1.125	0.0095	6.6
$m_4 = 278 \pm 10$	8.5×10^{-9}	0.011	1.145	0.0093	9.4

$$u_{\text{diff}} = -\delta_{p,\text{CMC-solution}} \frac{(\varphi_{p,0} - \varphi_{p,\text{EOF}})}{2r_p} \quad (9)$$

$\varphi_{p,0}$ is the particle volume fraction at the beginning of drying and $\varphi_{p,\text{EOF}}$ at the end of film shrinkage. The evaporation rate was determined on the basis of the experimental drying rates (\dot{m}_s) summarized in Table 5 for the different electrode area weights after Equation (10).

$$u_{\text{evap}} = \frac{\dot{m}_s}{\rho_s} \quad (10)$$

The results are summarized in Table 4. When comparing the velocities of diffusion and sedimentation with that of evaporation, it becomes clear that the evaporation rate clearly dominates and a consolidation layer at the top of the electrode might be present. For thin electrodes, though, the maximum distance a graphite particle might move to its final position is twice its diameter. The thicker the electrode is, the longer is the distance, and the effect of the high evaporation rate gains in importance. The CMC concentration in water increases from 1.5% at the beginning to 2.8–3% at the end of film shrinkage. In theory, this would result in an increase of the zero shear viscosity from around 21.7 Pa s to a factor of 20 to 40 times its viscosity.

An increase of the viscosity leads to even lower values of K_C and a higher tendency for the formation of a consolidation layer is expected. This supports the explanation for the detection of empty pores at the bottom even before the end of film shrinkage is reached and shows that initial film thickness influences the mechanisms governing electrode drying.

The question arises whether the film thickness influences the drying behavior in total, which is in part answered by the previous explanation of capillary pore emptying given by the digital microscope images. Another aspect in terms of the evaporation rate over drying time is addressed by the gravimetric measurement setup and discussed in the following section.

4.2.4. Visualization of Drying Patterns During Drying of Electrodes with Differing Thickness

In Figure 8, the drying patterns of the different area weight electrodes are compared. The electrode bottom images are compared at the theoretical end of film shrinkage and at a time before and after. For the thinnest electrode, a homogeneously distributed pore emptying seems to be present, whereas inhomogeneous

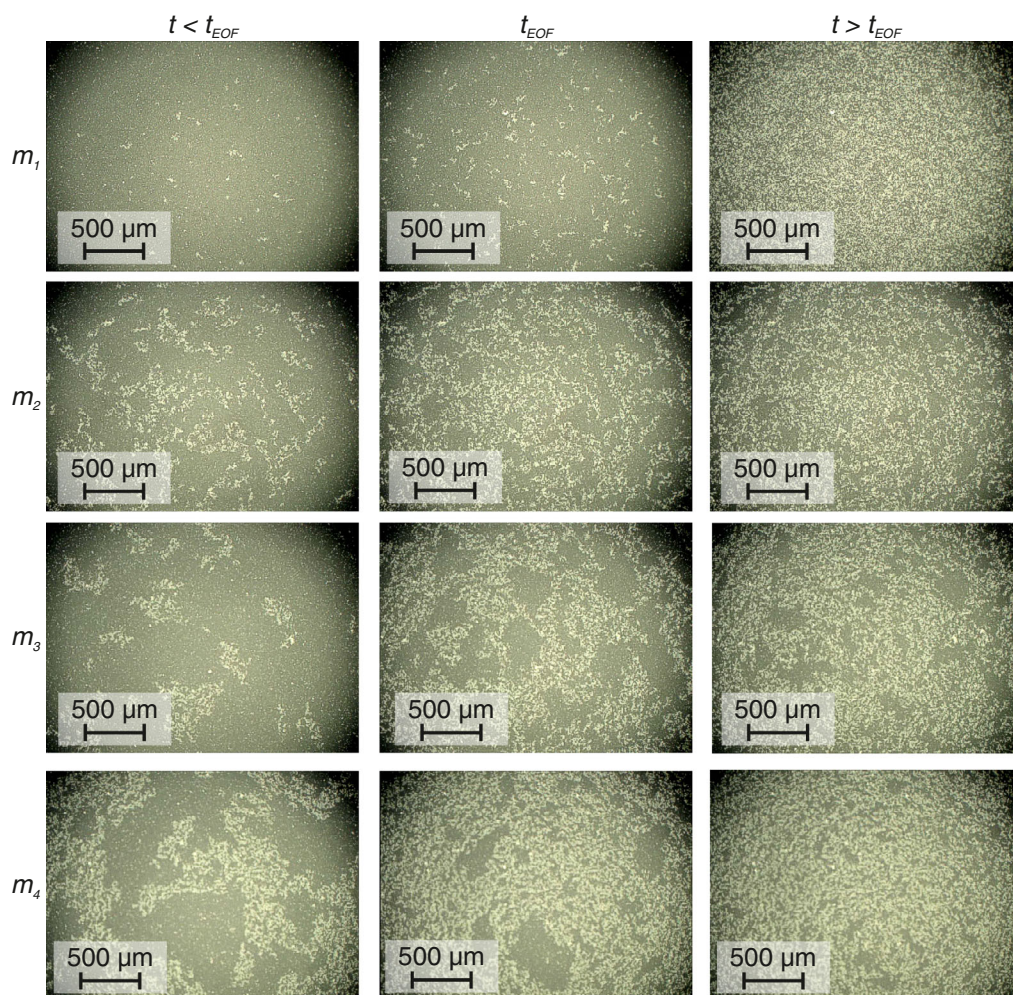


Figure 8. Comparison of the pore-emptying pattern of different area weight electrode films at different times of drying.

patterns appear during the drying of all higher thicknesses. It can thus be inferred that at higher film thicknesses capillary transport is partly interrupted due to an increasingly inhomogeneous distribution of the capillaries within the electrode. Thus, the capillary transport cannot be assumed to maintain a high drying rate during the drying of electrodes with area weights above the lowest investigated value of $m_1 = 72 \text{ g m}^{-2}$. A consolidation layer, forming during electrode drying, might influence the start of the film side controlled mass transport resistance development.^[5]

4.3. Experimental Validation of the Simulation Model

Using the simulation introduced in a previous work and the moving drying front model based on Krischer as explained in Section 3, drying curves of electrodes of four different area weights m_1 to m_4 were simulated and compared to the experiments as shown in Figure 9.^[5,16] It was assumed for all area weights that a resistance due to the meniscus of the uppermost capillary moving into the film would build up at the theoretical end of film shrinkage. This point was chosen as a first assumption due to the theoretical accessibility and the resulting easy

implementation into the simulation, without the necessity of further experiments. As a stationary dryer with a variable heat transfer coefficient was utilized for the experimental validation, the simulation considers the heat transfer coefficient distribution for both solvent loading and temperature calculations; it is referred to as “accum. α -distribution.” The shaded area in all graphs thereby describes the possible range of solvent loading and temperature caused by the α -distribution. It is compared to a simulation using only the most frequent value of the heat transfer coefficient, called “ α -median.” The medium value of the heat transfer coefficient of the dryer $\alpha_{\text{top,linreg}}$ during the experiments was determined using the initial slope of the experimental solvent loading curve $\dot{m}_{\text{s,exp}} = \frac{\Delta X}{\Delta t} \frac{M_{\text{el}}}{A_{\text{el}}}$. From the Lewis number $Le_{\text{s,air}}$, the heat capacity of air $\tilde{c}_{\text{p,air}}$, the Stefan correction K_{St} , the molar mass of the solvent M_{s} , and the solvent molar fraction at the interface $\tilde{y}_{\text{s,ph}}$ and in the gas phase $\tilde{y}_{\text{s,g}}$, respectively, the corresponding heat transfer coefficient $\alpha_{\text{top,linreg}}$ can be calculated according to Equation (11).

$$\alpha_{\text{top,linreg}} = \frac{\dot{m}_{\text{s,exp}} Le_{\text{s,air}}^{1-n} \tilde{c}_{\text{p,air}}}{K_{\text{St}} \tilde{M}_{\text{s}} (\tilde{y}_{\text{s,ph}} - \tilde{y}_{\text{s,g}})} \quad (11)$$

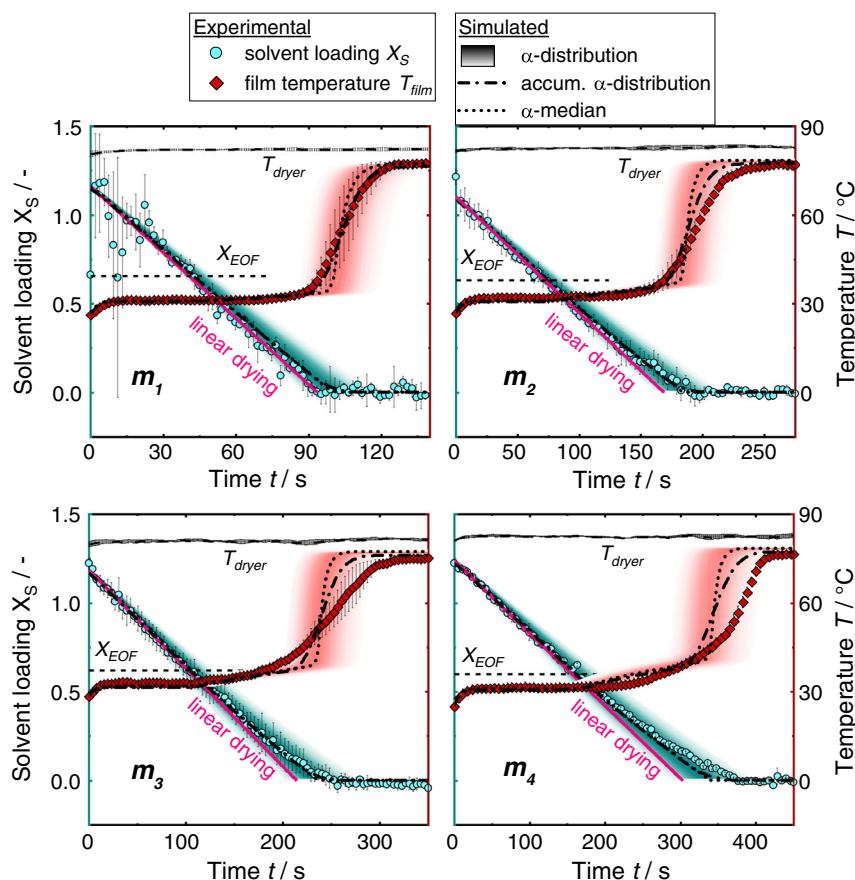


Figure 9. Experimental and simulated drying curves of electrodes of four different area weights m_1 to m_4 . The experimental data of m_1 (upper left) have been previously published.^[16]

The experimentally determined heat transfer coefficients, drying rates, and steady state temperatures for all four area weights are summarized in **Table 5**.

The solvent loading simulation for the electrode with the lowest area weight m_1 shows good agreement with the experimental values up to 75% of the total drying time. Around that point a deviation from the experimental data can be observed, which is then better described by linear drying kinetics that neglect a film resistance. The temperature curve can be described quite well by the simulation in terms of the steady state temperature as well as the equilibrium end temperature. The onset of the

Table 5. Experimentally determined drying parameters of the four electrodes, which were dried in the gravimetric setup sorted by their respective area weights.

Dry area weight m [g m ⁻²]	Heat transfer coefficient $\alpha_{\text{top,linreg}}$ [W m ⁻² K ⁻¹]	Drying rate \dot{m}_s [g m ⁻² s ⁻¹]	Steady state temperature $T_{\text{steady state}}$ [°C]
$m_1 = 72 \pm 5$	39.3	0.89	31.5
$m_2 = 160 \pm 12$	46.1	1.04	31.7
$m_3 = 201 \pm 1$	52.2	1.12	32.3
$m_4 = 278 \pm 10$	51.1	1.14	31.4

temperature rise lies well within the range of the error bars for the simulation with accum. α -distribution.

When comparing the experimental solvent loading with the simulated curves of the higher area weight m_2 , it becomes clear that both simulations accum. α -distribution and α -median, accounting for a film resistance, are able to describe the experimental data, whereas linear drying kinetics predict shorter drying times. This trend can also be observed for the two higher area weights m_3 and m_4 . The deviation between linear drying kinetics and the simulation using the moving drying front model steadily grows. The difference between the simulation accounting for the distribution of the heat transfer coefficient, and the one using only the median value is negligible. Although the prediction of the temperature curve fits better for the accum. α -distribution, the deviation from the experimental temperature values still grows with increasing area weight. One explanation might be the local temperature measurement compared to the integral simulation or the thermocouple influencing the actual measurement, as described in more detail in a previous work.^[16] Another reason could be the influence of the heat conductivity. The heat conductivity was calculated using the Zehner–Bauer–Schlünder model for a porous system consisting of graphite and air when reaching the EOF shrinkage.^[18] Because the real system undergoes a change

in porosity and there is also no clear boundary between the wet and dry electrode, the heat conductivity in the simulation is only an approximation to reality.

4.4. Comparison of the Simulation Models

To judge which model fits best, the two simulations using the moving drying front model and the one assuming linear drying kinetics were compared to the experimental data in **Figure 10**. Therefore, the predicted drying times were compared to the actual drying time. Since the model includes sorption data, the solvent loading never reaches a value of $X_S = 0$ but assumes the equilibrium solvent loading. Therefore, the times when 99% of the solvent has been removed in relation to the equilibrium solvent loading were compared. The exact times are summarized in **Table 6**.

When comparing the accuracy of the different models, it becomes clear that the linear drying kinetics best describe the drying behavior of electrodes with low area weight (state of

the art in industrial manufacturing). Here, the moving drying front models predict around 10 s longer drying times than the experimental data.

Already at an area weight of about a factor of two of the current state of the art, the linear drying kinetics fail to predict the end time of drying correctly. Both simulations including the moving drying front model show good agreement when predicting the overall drying time, with the accumulated α -distribution being slightly more precise. This is valid for all higher area weights. The error for the thickest electrodes with an absolute value of 25 s is a maximum of 6%, whereas the linear drying kinetics for the highest area weight lead to an error of more than 20% and an absolute error of 87 s. The comparison shows that a film resistance has to be taken into account for the drying of films with area weights exceeding state-of-the-art thickness. The model of Krischer thereby seems to be applicable, even though it constitutes only a simplified version of the actual drying process. The assumption of the resistance starting to build up at the EOF shrinkage seems to be justified, even though the experiments using the digital microscope show that first capillaries start to empty even before that point. Thus, the time when a film resistance starts to play a role seems not to coincide with the time when the first capillaries start to empty.

It can be assumed that the moving drying front model represents an averaged value of the actual drying behavior: As battery electrodes do not possess an ideal microstructure in terms of evenly distributed pores, small menisci reaching from the top to the bottom of the film are not evenly distributed as well. As a consequence, some menisci will stay saturated at the electrode's top as other capillaries break and menisci retreat into the film. Because the remaining capillaries do not suffice to maintain the solvent transport to the surface, the solvent menisci within the film start to dominate, thus reducing the drying rate. Although the model assumes a homogeneously retreating drying front, it is likely that a mixture between gas- and water-filled capillaries is present in the electrodes' microstructure with increasing area drying with a film resistance. The thicker the electrode, the more probable is the existence of disconnected solvent-filled clusters within the film that cannot be emptied by capillaries reaching to the film surface.

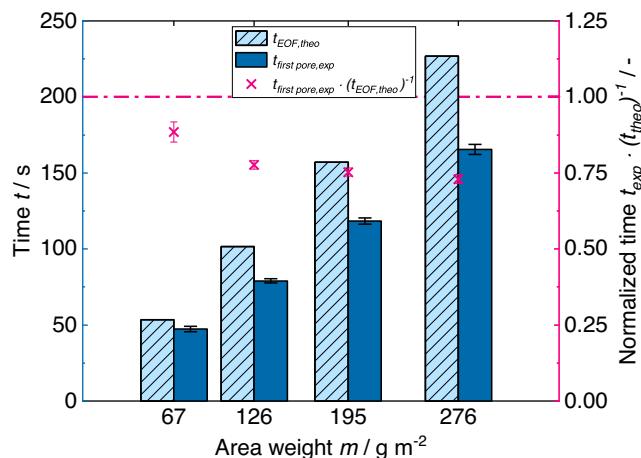


Figure 10. Comparison of drying times until the electrode reaches a solvent loading of 1% in relation to the equilibrium solvent loading. The times of the experimental data in relation to the simulation using linear drying kinetics and to the two simulations assuming the moving drying front (MDF) model are given.

Table 6. Summary of drying times until the electrode reaches a solvent loading of 1% in relation to the equilibrium solvent loading. The times of the experimental data are compared to the simulation using linear drying kinetics and to the two simulations assuming the MDF model.

Dry area weight m [g m^{-2}]	Exp. drying time $t_{\text{dry,exp}}$ [s]	Sim. drying time (MDF model, α -distr.) $t_{\text{dry,MDF},\alpha\text{-accum.}}$ [s]	Sim. drying time (MDF model, α -median) $t_{\text{dry,MDF},\alpha\text{-median}}$ [s]	Sim. drying time (linear model, α -median) $t_{\text{dry,linear}}$ [s]
$m_1 = 72 \pm 5$	94	108	102	94
$m_2 = 160 \pm 12$	203	210	198	168
$m_3 = 201 \pm 1$	257	275	260	214
$m_4 = 278 \pm 10$	389	400	378	302

5. Conclusion

In this investigation a model was successfully used to predict the drying curves of battery electrodes of different area weights. The model used for the simulation assumes a solvent receding into the film, and the solvent thus being subject to a mass transport resistance. Heat transport changes only slightly due to the main dependency of heat transport on the graphite particles surrounded first by the solvent and at one point by air. The solvent loading at which the water front starts to recede into the film was assumed to be the one at the EOF shrinkage. In a preceding experiment using a digital microscope, the drying mechanisms were explained. The first empty pore at the bottom of the film was observed during drying. For thin electrode films, it could be shown that the time of the first empty pore breaking through to the bottom of the film and the EOF shrinkage almost coincide. The thicker the electrode is though, the earlier the breakthrough

of the first pore compared to the theoretical EOF shrinkage is observed. These findings clearly show that capillary transport governs drying, and that capillary conduction of the solvent can start even before the EOF shrinkage, and therefore before the particles are arranged at their most dense packing. One explanation for this observation might be the appearance of a particle consolidation layer at the top of the film, forming a denser particle packing and thus smaller pores for capillary transport. Even though the simulation does not include capillary transport and a model of the evolving pore geometry, it is able to predict the EOF drying with a maximum error of 6% for thick electrodes. As capillary pressure is highest in the smallest capillaries, these will stay solvent-filled while pulling the solvent away from cavities or thicker capillaries within the microstructure. As shown by the experiment using the digital microscope, this effect should be present quite early during drying, depending on the film thickness. The higher is the film thickness, the higher is the probability that capillaries break and disconnect from the rest of the solvent-filled microstructure. At one point during drying, the surface menisci are no longer connected to solvent reservoirs within the microstructure, and move inward due to evaporation, leading to transport limitations within the film. For the case that capillary transport starts before the theoretical EOF shrinkage, it can be reasoned that the actual end of film shrinkage lies behind the theoretically calculated one because the solvent evaporates from the inner pore structure, which does not necessarily lead to an approximation of the particles. It becomes clear that the proposed model does not account for the real solvent movement within the capillaries, but it reflects an averaged value of pores receding into the film, which sufficiently predicts actual drying times.

Acknowledgements

The authors would like to thank the students involved in this work: L. Eyman and V. Francesconi. The authors acknowledge the financial support of the Federal Ministry of Education and Research (BMBF) within the "ProZell" cluster project "High Energy" under the reference number 03XP0073B. Part of the experimental setup used in this work was financed by the German Research Foundation DFG GZ 1266/9-3. This work contributes to the research performed at the Center for Electrochemical Energy Storage Ulm-Karlsruhe (CELEST).

Open access funding enabled and organized by Projekt DEAL.

Conflict of Interest

The authors declare no conflict of interest.

Data Availability Statement

Research data are not shared.

Keywords

drying, graphite anodes, gravimetric drying curves, lithium-ion batteries, thick electrodes

Received: January 7, 2021

Revised: March 3, 2021

Published online:

- [1] M. Müller, L. Pfaffmann, S. Jaiser, M. Baunach, V. Trouillet, F. Scheiba, P. Scharfer, W. Schabel, W. Bauer, *J. Power Sources* **2017**, *340*, 1.
- [2] L. Pfaffmann, S. Jaiser, M. Müller, P. Scharfer, W. Schabel, W. Bauer, F. Scheiba, H. Ehrenberg, *J. Power Sources* **2017**, *363*, 460.
- [3] J. Kumberg, M. Müller, R. Diehm, S. Spiegel, C. Wachsmann, W. Bauer, P. Scharfer, W. Schabel, *Energy Technol.* **2019**, *3*, 1900722.
- [4] E. W. Comings, T. K. Sherwood, *Ind. Eng. Chem.* **1934**, *26*, 1096.
- [5] O. Krischer, *Die wissenschaftlichen-Grundlagen-der-Trocknungstechnik*, Springer-Verlag, Berlin Heidelberg GmbH **1956**.
- [6] E.-U. Schlünder, *Chemie Ingenieur Technik* **1988**, *60*, 117.
- [7] E.-U. Schlünder, *Drying Technol.* **2004**, *22*, 1517.
- [8] M. Prat, *Int. J. Multiphase Flows* **1993**, *19*, 691.
- [9] T. Metzger, E. Tsotsas, *Drying Technol.* **2005**, *23*, 1797.
- [10] T. Metzger, A. Irawan, E. Tsotsas, *Drying Technol.* **2007**, *25*, 49.
- [11] T. Metzger, A. Irawan, E. Tsotsas, *AIChE J.* **2007**, *53*, 3029.
- [12] T. Metzger, E. Tsotsas, *Chem. Eng. Res. Des.* **2008**, *86*, 739.
- [13] T. Metzger, E. Tsotsas, *Chemie Ingenieur Technik* **2010**, *82*, 869.
- [14] T. Metzger, *Drying Technol.* **2018**, *37*, 497.
- [15] M. Börnhorst, P. Walzel, A. Rahimi, A. Kharaghani, E. Tsotsas, N. Nestle, A. Besser, F. Kleine Jäger, T. Metzger, *Drying Technol.* **2016**, *34*, 1964.
- [16] J. Kumberg, M. Baunach, J. C. Eser, A. Altvater, P. Scharfer, W. Schabel, *Energy Technol.* **2020**, *3*, 2000889.
- [17] J. C. Eser, T. Wirsching, P. G. Weidler, A. Altvater, T. Börnhorst, J. Kumberg, G. Schöne, M. Müller, P. Scharfer, W. Schabel, *Energy Technol.* **2019**, *73*, 1801162.
- [18] VDI-Wärmeatlas: Tsotsas, E. "D6. 3 Wärmeleitfähigkeit in Schüttschichten." VDI-Wärmeatlas, Springer **2013**, pp. 651–660.
- [19] S. Jaiser, L. Funk, M. Baunach, P. Scharfer, W. Schabel, *J. Colloid Interface Sci.* **2017**, *494*, 22.
- [20] M. Baunach, S. Jaiser, S. Schmelzle, H. Nirschl, P. Scharfer, W. Schabel, *Drying Technol.* **2015**, *34*, 462.
- [21] S. Baesch, P. Scharfer, W. Schabel, L. Francis, *J. Compos. Mater.* **2017**, *51*, 3391.
- [22] V. C.-A. Gracia-Medrano-Bravo, J. Gröne, S. Baesch, P. Scharfer, W. Schabel, *Langmuir: ACS J. Surfaces Colloids* **2020**, *36*, 6245.